



University
of Glasgow

Viale, A. , Bailet, G. , Ceriotti, M. and McInnes, C. (2021) Excavation of artificial caverns inside asteroids by leveraging rotational self-energy. *Advances in Space Research*, 67(12), pp. 4142-4157.

(doi: [10.1016/j.asr.2021.02.021](https://doi.org/10.1016/j.asr.2021.02.021))

This is the Author Accepted Manuscript.

There may be differences between this version and the published version. You are advised to consult the publisher's version if you wish to cite from it.

<https://eprints.gla.ac.uk/234471/>

Deposited on: 18 February 2021

Excavation of artificial caverns inside asteroids by leveraging rotational self-energy

Andrea Viale^{a,*}, Gilles Baillet^a, Matteo Ceriotti^a and Colin McInnes^a

^aJames Watt School of Engineering, University of Glasgow, Glasgow (UK)

ARTICLE INFO

Keywords:

Asteroid mining, asteroid engineering, orbital siphon, space resources

ABSTRACT

Future space ventures will likely require exploitation of near-Earth asteroid resources. Moreover, it can be envisaged that asteroids may host habitats in their interiors. In fact, a cavern inside an asteroid would be a natural radiation shield against cosmic radiation and may also serve as a confined environment for storage of mined material such as water ice or other processed volatiles such as propellants. To this end, this paper proposes to leverage the asteroid rotational self-energy to remove material from the asteroid interiors and create a spherical cavern, by means of the orbital siphon concept. The siphon is a chain of tether-connected payload masses (the asteroid material), which exploits the rotation of the asteroid for the delivery of mass from the asteroid to escape. Under certain conditions the siphon can be initiated to ensure self-sustained flow of mass from the asteroid to escape. A net orbital siphon effect is generated by connecting new payloads at the bottom of the chain while releasing the upper payloads. Key parameters are discussed, such as the required siphon dimension and the maximum size of the internal cavity that can be excavated, as a function of the asteroid rotational period. Moreover, assuming elastic material behaviour, a close-form expression for the stress tensor is found and a failure criterion is used to identify regions in the asteroid interiors subjected to the larger stresses. It is shown that the conditions for failure are relaxed as the radius of the internal void increases.

1. Introduction and motivation

Interest in asteroids, in particular near-Earth asteroids, has been growing significantly in the past decades. Several studies have confirmed that many of these objects are abundant in useful resources, such as water, metal, and semi-conductors (Gerlach, 2005). Moreover, a significant fraction of the near-Earth asteroid population is accessible at relatively low energy (Sanchez and McInnes, 2012). Future space ventures will likely require large quantities of mass to be launched (for example, to build infrastructures): the ability to exploit material already available in space would in principle offer significant savings with respect to launching the required resources from Earth. Also, future space ventures will likely involve the development of human space settlements. To this end, artificially hollowed asteroids would represent a viable solution for developing space habitats, for a number of reasons. Among the main requirements for long term sustainability of life in space are radiation shielding and artificial gravity. Internal asteroid caverns would provide a natural protection against cosmic rays and solar wind. Contrary to other habitat concepts (such as O'Neill cylinders at the Lagrangian points O'Neill and O'Leary (1977)), an advantage of asteroids is that material for shielding is already available *in situ* and does not have to be sourced elsewhere. According to a study by Harris, Hershers, Hofhammer and Jenkin (2014) the minimum level of gravity to provide adequate perception of the upright direction for humans is approximately 0.15 g. In addition, there are constraints due to tolerable levels of Coriolis acceleration (Hennion and Mollard, 1993). Two main methods have been proposed to simulate artificial gravity. The first consists in spinning up the entire asteroid such that the required level of artificial gravity is obtained on the lateral surface of an internal cylindrical cavity (Maindl, Miksch and Loibnegger, 2019). However, rotation periods on the order of 1 minute are required to generate 0.15 g on a cylindrical cavern with radius of 100 m (Maindl et al., 2019) and

*Corresponding author
ORCID(s):

the asteroid may not sustain the body loads due to the rotation rate. In fact, most asteroids with size above a hundred meter radius are believed to be gravity-dominated rubble piles with zero or negligible tensile strength (Pravec and Harris, 2000). Also, asteroid rotation periods are usually above 2.2 hours (Pravec and Harris, 2000) and the spin up process may require significant energy due to the large inertia of the body. An alternative method to generate artificial gravity would be to spin up a cylindrical or toroidal structure inside the cavity (Maindl et al., 2019). In this way, the rotation of the space habitat is decoupled from that of the asteroid and therefore the requirement to spin up the entire asteroid is eliminated. Moreover, the microgravity environment at the outer asteroid surface is preserved, which may be advantageous for manufacturing infrastructures.

Furthermore, excavation of asteroid interiors would be beneficial in a mining scenario if the resources to be processed are naturally at a certain depth from the surface. For example, in C-type asteroids, water may be available in the form of fluid inclusions (Saylor, Zolensky, Bodnar, Le and Schwandt, 2001) and may also be trapped underneath the surface, where the thermal inertia is larger and the diurnal variation of temperature becomes negligible, so that water does not evaporate. Also, in the low-gravity environment of the asteroid, an internal cavern would offer a confined environment for storage of mined or processed material, such as propellant manufactured from asteroid-mined water. The material removed from the asteroid may also be used as reaction mass to change the asteroid orbit. This can be achieved either via mass drivers (Dunn, Fagin, Snyder and Joyce, 2017) or tethered systems (Viale, McInnes, Bailet and Ceriotti, 2020b). More speculatively, the internal cavity may be pressurised to facilitate the disruption of the asteroid. This would increase the surface to volume ratio of the asteroid and may be useful to harvest water, for example using solar concentrator technology (McInnes, 2017).

To this end, this paper proposes to leverage the asteroid rotational self-energy to create an artificial cavern inside a spherical asteroid, by means of the orbital siphon concept. The siphon, initially devised by Davis (McInnes and Davis, 2005) and extensively studied by the authors in previous publications (Viale, McInnes and Ceriotti, 2018a, 2020c; Viale, Ceriotti and McInnes, 2020a; Viale, McInnes and Ceriotti, 2018b) is a chain of tethered connected payload masses (in this case, the asteroid material) arranged vertically from the asteroid surface beyond the synchronous orbit radius: if the chain is long enough, the centrifugal pull due to the body's spin will overcome the gravitational force on the payloads, thus allowing the chain to lift (Viale et al., 2018a). An orbital siphon effect can then be envisaged if new payloads are connected at the bottom of the chain and top payloads are released. In previous papers, the orbital siphon was anchored at a point on the asteroid equator. In the scenario studied in this paper, an artificial tunnel excavated from the asteroid equator to its center contains the orbital siphon, extending from the asteroid interior to orbit. Mining units would then excavate material from the asteroid interiors and use the siphon as a conveyor for releasing extracted material to escape. Similar to (Viale et al., 2018a) the dynamical effects of long term mass removal are considered. In particular, it is shown that the asteroid period gradually increases during siphon operation: this implies that the maximum internal volume that can be created using the siphon effect depends on the initial angular velocity of the asteroid.

The paper is divided in two parts. In the first part the theory of orbital siphons developed by Viale et al. (2018a) is applied to this scenario. Relevant performance parameters and requirements are calculated and discussed, such that extraction time, maximum volume of the internal cavity and mass flow rates. In the second part, the variation of the internal asteroid stresses resulting due to the internal void is analyzed. Assuming elastic material behavior and using stress-free boundary conditions, a closed-form solution to the stress tensor is found. Then, using the Druker-Prager yield criterion, regions inside the asteroid that are more sensitive to structural failure are identified.

2. Model

The asteroid is modelled as a sphere with radius R , uniform density ρ and angular velocity ω . An artificial tunnel, excavated from a point on the asteroid equator to its center, contains the orbital siphon, with length $L > R$ (Fig. 1). It is assumed that the cross section of the tunnel is small compared to the radius of the asteroid, hence the change of asteroid mass and inertia due to the presence of the

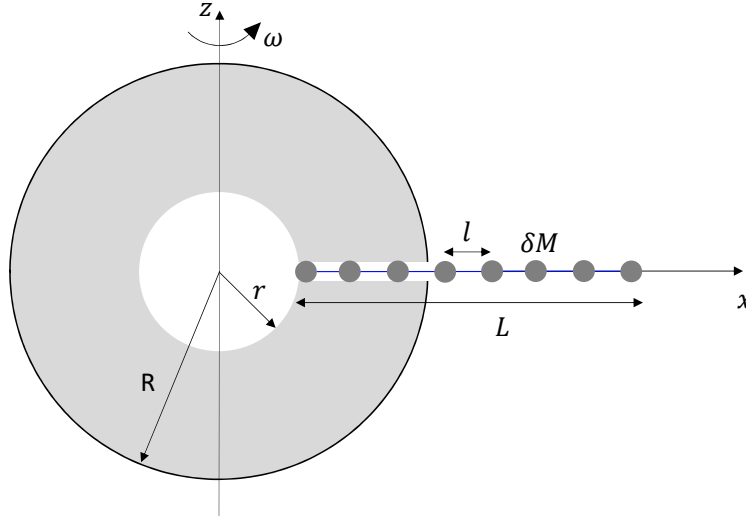


Figure 1: Orbital siphon model.

tunnel can be neglected. As in Ref. Viale et al. (2018a), the siphon is modelled as a chain of n tether-connected payload masses each with mass δM and the mass of the tethers is neglected. Mining units extract material from the asteroid interior and transfer it to the siphon. For simplicity, the internal cavity is assumed to be spherical, with time varying radius $r < R$. Specific modelling of the cavity initialization at $r = 0$ is outside the scope of this paper. However, it could be imagined that a narrow tunnel is drilled from the surface, and then enlarged at the centre of the asteroid to allow the siphon to be deployed and the excavation process to commence. The siphon is assumed to keep a fixed orientation, normal to the asteroid surface. This implies that the masses are sliding without friction on a support structure to avoid rotation of the siphon caused by the Coriolis acceleration resulting from the motion of the chain. Such a support structure can either be a rigid rod or a tether anchored at the base of the siphon and kept in tension via a counterweight (see Viale et al. (2018b, 2020a,b)).

2.1. Force on the siphon

Within an asteroid-fixed reference frame, each payload mass is subjected to a gravitational force directed towards the center of the asteroid and a centrifugal-induced force, in the opposite direction. Let $x_i = r + (i-1)l$ be the distance between the i -th payload mass and the center of the asteroid, where $l = L/(n-1)$ is the constant length of the tethers connecting consecutive payloads. The gravitational and centrifugal-induced forces can be written respectively as:

$$f_{g,i} = \begin{cases} -G\frac{4}{3}\pi\rho\frac{x_i^3 - r^3}{x_i^2}\delta M, & \text{if } x_i \leq R \\ -G\frac{4}{3}\pi\rho\frac{R^3 - r^3}{x_i^2}\delta M, & \text{if } x_i > R \end{cases} \quad (1)$$

and

$$f_{c,i} = \delta M\omega^2 x_i \quad (2)$$

where $G = 6.67 \times 10^{-11} \text{ m}^3 \text{ kg}^{-1} \text{ s}^{-2}$ is the gravitational constant. The gravitational force for points inside the sphere follows from Newton's shell theorem Newton (1687). Then, the total force acting

Table 1: Scale factors for non-dimensional variables

Scale factors	
Distance	R
Mass	M_0
Time	ω_c^{-1}
Angular velocity	ω_c
Velocity	$\omega_c R$
Force	$M_0 \omega_c^2 R$

on the siphon will be the sum

$$f = \sum_{i=1}^n (f_{g,i} + f_{c,i}) \quad (3)$$

Internal tether tensions are not explicitly listed in Eq. (3) as they will vanish in a summation to be performed later. From this point Equation (3) can then be written in non-dimensional form by scaling masses, distances and angular velocity by M_0 , R and $\sqrt{4/3\pi\rho G}$ respectively, where M_0 is the initial mass of the asteroid:

$$\bar{f} = \left(\bar{\omega}^2 x_i - \sum_{i=1}^{n^*} \frac{\bar{x}_i^3 - \bar{r}^3}{\bar{x}_i^2} - \sum_{i=n^*+1}^n \frac{1 - \bar{r}^3}{\bar{x}_i^2} \right) \delta \bar{M} \quad (4)$$

where the upper bar indicates a non-dimensional variable. The angular velocity scaling factor $\omega_c = \sqrt{4/3\pi\rho G}$, here termed the *critical angular velocity* in analogy with Refs. Viale et al. (2018a, 2020a,b,c), corresponds to the asteroid spin at which the gravitational and centrifugal-induced acceleration are balanced at the equator, when $r = 0$. The resulting force scaling factor is $M_0 \omega_c^2 R$. Table 1 shows the scale factors used in this paper. The variable n^* represents the number of payload masses below the asteroid surface, i.e., the largest positive integer verifying:

$$r + (n^* - 1)l < 1 \quad (5)$$

Upon simplification, Eq. (4) can be written as:

$$\bar{f} = \frac{\delta \bar{M}}{\bar{l}^2} \left[\bar{r}^3 \Psi \left(1 + \frac{\bar{r}}{\bar{l}} \right) + (1 - \bar{r}^3) \Psi \left(n + \frac{\bar{r}}{\bar{l}} \right) - \Psi \left(n^* + \frac{\bar{r}}{\bar{l}} \right) \right] + \frac{\delta \bar{M}}{2} [n(\bar{L} + 2\bar{r}\bar{\omega}^2 - (\bar{l}n^* + 2\bar{r})(n^* - 1))] \quad (6)$$

where $\psi(\xi)$ is the polygamma function of order 1 defined in series as Abramowitz and Stegun (1964)

$$\psi(\xi) = \sum_{i=0}^{\infty} (\xi + i)^{-2} \quad (7)$$

When the condition

$$\bar{f} = 0 \quad (8)$$

is verified, the total gravitational and centrifugal-induced forces are balanced and the chain is in equilibrium. Figure 2 shows the variation of the function $\bar{f}/\delta \bar{M}$ with respect to the siphon length \bar{L} , for an asteroid with $\bar{\omega} = 0.7$, $n = 30$ and a range of inner radii \bar{r} . It is apparent that, for a given $\bar{\omega}$, n and \bar{r} , two equilibria exist. The smaller equilibrium corresponds to a siphon entirely contained within

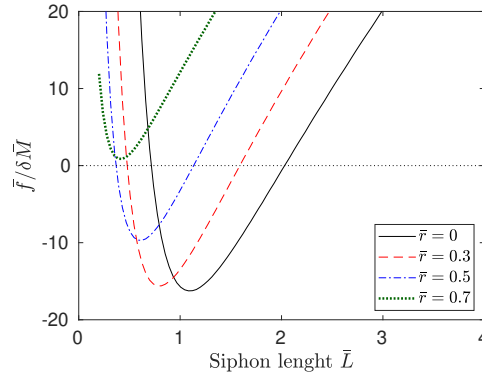


Figure 2: Non-dimensional siphon force as a function of the siphon length, for $\bar{\omega} = 0.69$, $n = 30$ and a range of inner radii r .

the tunnel, i.e., with its top mass below the asteroid surface. The larger equilibrium corresponds to a siphon extending outside the asteroid surface. If the radius of the inner void is larger than a certain threshold, which depends on $\bar{\omega}$ and n , the siphon force is always positive and no equilibrium exists. It can be shown that the inner equilibrium is stable in the radial direction whereas the outer equilibrium is unstable. This implies that an orbital siphon effect cannot be generated for a sub-surface orbital siphon. Additionally, a sub-surface orbital siphon would not release top masses outside the asteroid, and would not be suitable for mass extraction purposes. Therefore, only siphons extending outside the asteroid surface are here considered.

2.1.1. Approximation for a continuous chain

It is useful for analyses to be performed later to rewrite Eq. (6) by approximating the siphon with a continuous mass distribution with the same length L and linear density $\mu = n\delta M/L$. This is obtained by substituting the sum in Eq. (3) with an integral over the length of the siphon. It can be shown that, under these conditions, the total force can be written in non-dimensional form as

$$\bar{f}_{\text{cont}} = \left[\frac{(\bar{r} - 1)(\bar{r}^2 + \bar{r} - 2 + 3\bar{L}(\bar{r} + 1))}{\bar{L} + \bar{r}} + \bar{L}(\bar{L} + 2\bar{r})\bar{\omega}^2 \right] \bar{\mu} \quad (9)$$

where the non-dimensional parameter $\bar{\mu}$ represents the ratio between the mass of a siphon with length $L = R$ and the mass of the asteroid M_0 . Figure 3 shows the siphon equilibrium length L_{eq} as a function of the non-dimensional asteroid angular velocity $\bar{\omega}$ using the continuous mass distribution approximation (continuous lines), compared with the discrete chain case (dashed lines and dotted lines, corresponding to $n = 10$ and $n = 30$ respectively) for a range of inner radii \bar{r} . It is apparent that the equilibrium solution found with the continuous mass distribution approach is an accurate approximation of the discrete chain case. As expected, the equilibrium length decreases with larger asteroid angular velocity. Moreover, a larger internal cavity reduces the asteroid mass and also the gravitational force acting on the chain, thus decreasing the equilibrium length.

2.2. Siphon operation: conservation of angular momentum

If the net force on the siphon is positive the chain will lift and an orbital siphon effect can be envisaged, where new payloads are connected at the bottom of the chain while upper payloads are released McInnes and Davis (2005); Viale et al. (2018a). In analogy with Ref. Viale et al. (2018a), the extraction of a payload mass from the asteroid and the subsequent release of the top payload mass from the chain can be modelled through the following four-step sequence (see Fig. 4):

1. The chain is initially in the configuration (1) with $x_1 = r$ and will subsequently lift if $f > 0$
2. The chain is in the configuration (2), with $x_1 = r + l$.

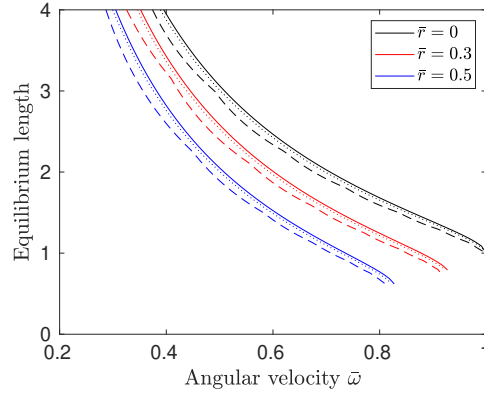


Figure 3: Equilibrium length (non-dimensional units) of the siphon as a function of the non-dimensional angular velocity $\bar{\omega}$ for a range of inner radii \bar{r} , using the continuous mass distribution approximation (continuous lines), compared with the discrete chain case (dashed lines and dotted lines, corresponding to $n = 10$ and $n = 30$)

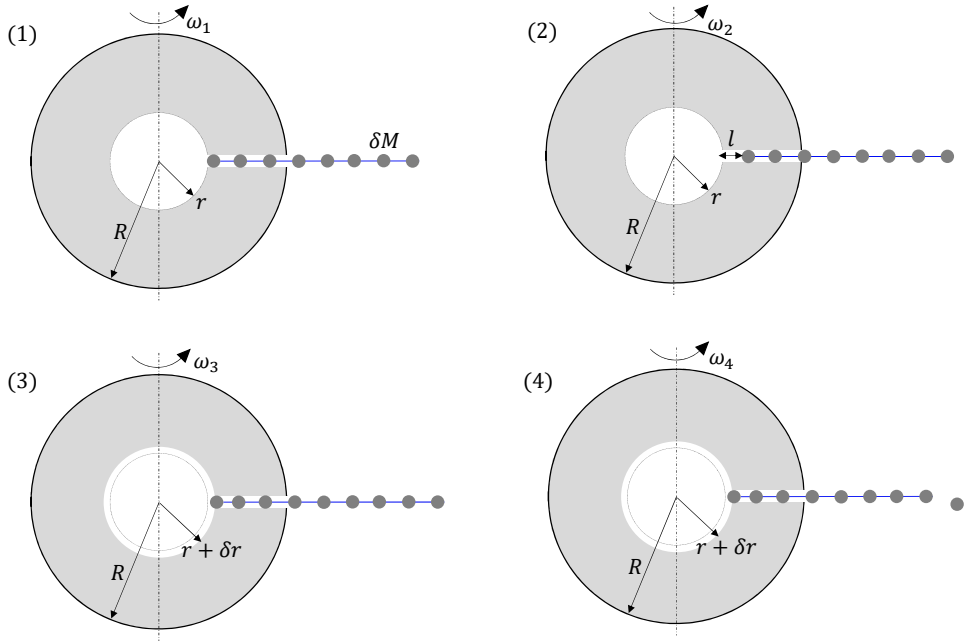


Figure 4: Siphon operation sequence

3. A new payload mass δM is connected at the bottom of the siphon. To guarantee conservation of mass, the inner radius r increases by $\delta r > 0$ such that, the mass of the outer shell with thickness δr is equal to δM .
4. The top mass is released from the chain.

The sequence is then repeated. Let r_j , M_j , $I_{A,j}$, $I_{S,j}$ and ω_j be the inner radius, asteroid mass, asteroid inertia, siphon inertia and asteroid angular velocity at the j -th step of the sequence described above. Then:

$$I_{A,j} = \frac{2}{5} M_j \frac{R^5 - r_j^5}{R^3 - r_j^3} \quad (10)$$

and

$$I_{S,j} = \begin{cases} \delta M \sum_{i=1}^n (r_j + (i-1)l)^2, & j = 1 \\ \delta M \sum_{i=1}^n (r_j + il)^2, & j = 2 \\ \delta M \sum_{i=1}^{n+1} (r_j + (i-1)l)^2, & j = 3 \\ \delta M \sum_{i=1}^n (r_j + (i-1)l)^2, & j = 4 \end{cases} \quad (11)$$

where $M_1 = M_2 = M$, $M_3 = M_4 = M - \delta M$ and $r_1 = r_2 = r$, $r_3 = r_4 = r + \delta r$.

Following Viale et al. (2018a), as no external torques are acting on the asteroid and chain, conservation of angular momentum holds at each step. Therefore:

$$(I_{A,1} + I_{S,1})\omega_1 = (I_{A,2} + I_{S,2})\omega_2 \quad (12a)$$

$$(I_{A,2} + I_{S,2})\omega_2 = (I_{A,3} + I_{S,3})\omega_3 \quad (12b)$$

$$(I_{A,3} + I_{S,3})\omega_3 = (I_{A,4} + I_{S,4})\omega_4 + \delta M(r_4 + nl)^2\omega_3 \quad (12c)$$

Substituting Eqs. (10) and (11) into Eq. (12) and further simplifying (see Appendix A for details) Eqs. (12) can be written as:

$$\frac{\delta\bar{\omega}_{12}}{\bar{\omega}_1} = 5 \frac{\bar{r}^5}{1 - \bar{r}^5} \left[\frac{3}{2} \left(1 + \frac{\bar{L}}{\bar{r}} \right)^2 - \frac{1}{2} \right] \frac{\delta\bar{r}}{\bar{r}} \quad (13a)$$

$$\frac{\delta\bar{\omega}_{23}}{\bar{\omega}_1} = -\frac{5}{2} \frac{\bar{r}^5}{1 - \bar{r}^5} \frac{\delta\bar{r}}{\bar{r}} \quad (13b)$$

$$\frac{\delta\bar{\omega}_{34}}{\bar{\omega}_1} = 0 \quad (13c)$$

where $\delta\bar{\omega}_{12} = \bar{\omega}_2 - \bar{\omega}_1$, $\delta\bar{\omega}_{23} = \bar{\omega}_3 - \bar{\omega}_2$, $\delta\bar{\omega}_{34} = \bar{\omega}_4 - \bar{\omega}_3$ and the higher-order terms are neglected. Again neglecting high-order terms:

$$\frac{\delta\bar{\omega}_{23}}{\bar{\omega}_2} = \frac{\delta\bar{\omega}_{23}}{\bar{\omega}_1 - \delta\bar{\omega}_{12}} = \frac{\delta\bar{\omega}_{23}}{\bar{\omega}_1} \left(1 + \frac{\delta\bar{\omega}_{12}}{\bar{\omega}_1} \right) = \frac{\delta\bar{\omega}_{23}}{\bar{\omega}_1}. \quad (14)$$

and equivalently

$$\frac{\delta\bar{\omega}_{34}}{\bar{\omega}_3} = \frac{\delta\bar{\omega}_{34}}{\bar{\omega}_1} \quad (15)$$

Hence, each contribute given by Eqs. (13) can be added to find the overall angular velocity variation $\delta\bar{\omega} = \delta\bar{\omega}_{12} + \delta\bar{\omega}_{23} + \delta\bar{\omega}_{34}$ between step 1 and 4:

$$\frac{\delta\bar{\omega}}{\bar{\omega}} = 5 \frac{\bar{r}^5}{1 - \bar{r}^5} \left[\frac{3}{2} \left(1 + \frac{\bar{L}}{\bar{r}} \right)^2 - 1 \right] \frac{\delta\bar{r}}{\bar{r}} \quad (16)$$

Note that the right-hand side of Eq. (12) only depends on the inner radius \bar{r} and on the length \bar{L} of the chain.

2.3. Siphon radial velocity

It was shown by Viale et al. (2018a) that the momentum exchange between the mass to be connected to the chain and the rest of the chain induces a deceleration of the siphon which eventually causes the siphon to reach a bound steady state velocity. For a siphon modelled as continuous mass distribution, the steady state velocity can be expressed in non-dimensional form as in Viale et al. (2020b)

$$\bar{v} = \sqrt{\frac{\bar{f}_{\text{cont}}}{\bar{\mu}}} \quad (17)$$

where the force \bar{f}_{cont} is given by Eq. (9). Substituting Eq. (9) into Eq. (17) yields:

$$\bar{v} = \sqrt{\frac{(\bar{r} - 1)(\bar{r}^2 + \bar{r} - 2 + 3\bar{L}(\bar{r} + 1))}{\bar{L} + \bar{r}} + \bar{L}(\bar{L} + 2\bar{r})\bar{\omega}^2} \quad (18)$$

The velocity scale factor used in Eqs. (17), (18) is $\omega_c R$.

2.4. Energy of the released material

Following the analysis in Viale et al. (2018a), the energy per unit mass E of the material released at the top of the siphon can be expressed as:

$$E = -\frac{4}{3}G\rho\pi(R^3 - r^3)\frac{1}{r + L} + \frac{1}{2}[\omega^2(r + L)^2 + v^2] \quad (19)$$

where the two terms represent the gravitational and kinetic energy of released payload respectively. Equation (19) can be conveniently written in non-dimensional form as:

$$\bar{E} = -\frac{1 - \bar{r}^3}{1 + \bar{L}} + \frac{1}{2}[\bar{\omega}^2(r + \bar{L})^2 + \bar{v}^2] \quad (20)$$

Assuming two-body dynamics upon release, the sign of \bar{E} determines the fate of the released material, i.e., if it will escape the asteroid or be inserted in orbit around it. Figure 5 shows the region of positive (green) and negative (yellow) release energy. Also shown in red is the region where the siphon effect cannot be generated due to negative radial force, calculated using Eq. (9). The dotted black line is the continuation of the contour line $E = 0$ inside the $f < 0$ region. For $\bar{r} = 0$ material can only be released to escape, whereas for $\bar{r} > 0$, release to bound orbit is possible only below a maximum siphon length, depending on \bar{r} and the angular velocity of the asteroid. However, the next section will show that, if the siphon length is chosen to maximise the volume of the internal cavity, then material can only be released to escape.

2.5. Maximum internal volume

Equation (16) can be integrated from $\bar{\omega}_0$ to $\bar{\omega}_f$ (left-hand side) and from $\bar{r}_0 = 0$ to \bar{r}_f (right-hand side) to obtain the angular velocity variation of the system as a function of the radius of the internal cavity.

$$\frac{\bar{\omega}}{\bar{\omega}_0} = \exp(-I) \quad (21)$$

where

$$I = \int_0^{\bar{r}_f} 5 \frac{\bar{r}^4}{1 - \bar{r}^5} \left[\frac{3}{2} \left(1 + \frac{\bar{L}}{\bar{r}} \right)^2 - 1 \right] d\bar{r} \quad (22)$$

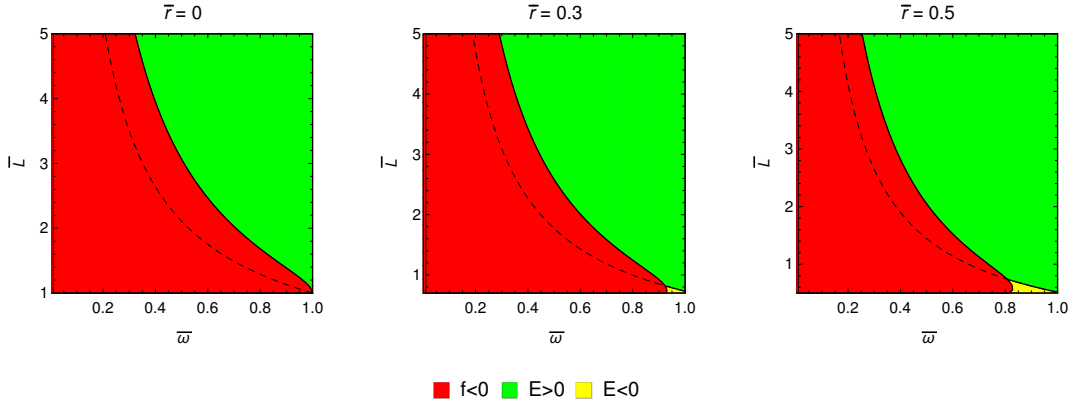


Figure 5: Regions of positive (green) and negative (yellow) energy of the material released from the siphon for a range of internal radii \bar{r} , as a function of the asteroid angular velocity $\bar{\omega}$ and the siphon length \bar{L} . Also shown in red is the region associated with negative siphon force, calculated using Eq. (9).

Since $\bar{I} > 0$ for any $\bar{L} > 0$ and $0 < \bar{r} < 1$, the angular velocity of the asteroid exponentially decreases as the radius of the internal cavity decreases. If the length of the siphon is constant, Eq. (21) admits a closed-form solution, however, due to the length of the resulting expression, it is not explicitly reported here. Then, for a given siphon initial angular velocity $\bar{\omega}_0$ and siphon length \bar{L} , the parameter $\bar{r}_{f,max} = \max(\bar{r}_f)$ verifying the condition $\bar{f} = 0$ (with the angular velocity calculated via Eq. (12)) represents the radius of the largest internal spherical cavity that can be excavated by exploiting the orbital siphon effect. Equivalently, $\bar{m}_f = \bar{r}_f^3$ represents the fraction of mass that has been removed, scaled with respect to the initial asteroid mass M_0 .

Figure 6a shows the extractable mass \bar{m}_f as a function of the siphon length \bar{L} for a range of initial asteroid angular velocities $\bar{\omega}_0$. As for the scenario analyzed in Viale et al. (2018a), an optimal siphon length which maximizes the extractable mass exists. As expected, the optimal chain increases with decreasing asteroid angular velocity: an asteroid with slower spin rate would require a larger chain to generate enough centrifugal pull to initialize the siphon effect. Figure 6b shows the maxima of Fig. 6a as a function of the asteroid initial angular velocity and the results are compared with that of Viale et al. (2018b). Viale et al. (2018b) analysed the case where material is mined from the surface of a spherical asteroid (rather than a spherical cavity as in the present study), with a siphon anchored at the asteroid equator. The maximum extractable mass for the internal siphon case is approximately 4.9% the initial mass of the asteroid for $\bar{\omega}_0 = 1$, corresponding to an internal spherical void of radius $\bar{r} = 0.36$, requiring a siphon length $\bar{L} = 1.28$. The maximum extractable mass for an external siphon is always larger, irrespective of $\bar{\omega}_0$. This is due to the fact that a siphon anchored at the asteroid equator benefits from a larger centrifugal-induced force and therefore the minimum length required to initialize the siphon effect is smaller. Hence the term $\delta\omega/\omega$ is smaller for a siphon anchored at the equator (compare Eq. (12) with Eq. 2.27 in Viale et al. (2018a)).

Figure 7 shows the non-dimensional energy of the released material as a function of the non-dimensional inner radius \bar{r} , for different asteroid initial angular velocities $\bar{\omega}_0$. The siphon length is chosen such that the extractable mass is maximised. It is apparent that for any $\omega_0 \leq 1$ material is always released to escape ($\bar{E} > 0$), i.e., release to bound orbits is not possible.

2.6. Timescale

The total time required to extract the mass \bar{m}_f is related to the siphon radial velocity and siphon linear density $\bar{\mu}$ via Viale et al. (2020b):

$$\bar{t} = \int_0^{\bar{m}_f} \frac{d\bar{m}}{\bar{\mu}\bar{v}} \quad (23)$$

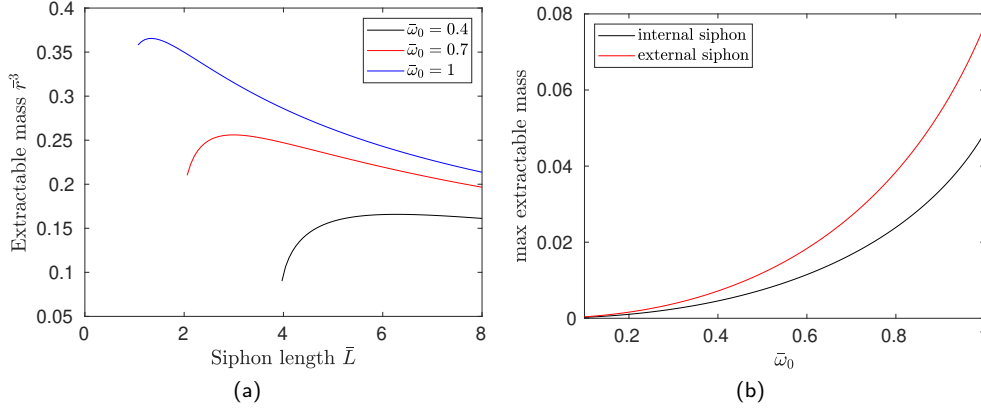


Figure 6: (a) Extractable mass as a function of the siphon length for a range of initial angular velocities. (b) Maximum extractable mass as a function of the initial angular velocity, compared with the results from Viale et al. (2018a), for a siphon anchored at the asteroid equator.

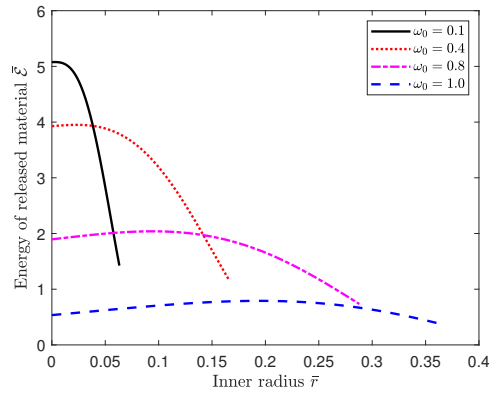


Figure 7: Non-dimensional energy $\bar{\mathcal{E}}$ of the released material as a function of the non-dimensional inner-radius \bar{r} , for different asteroid initial angular velocities $\bar{\omega}_0$. The siphon length is chosen such that the extractable mass is maximised.

for a siphon modelled as a continuous mass distribution. Similarly, the instantaneous mass rate of material lifted by the siphon is (Viale et al., 2020b):

$$\frac{d\bar{m}}{d\bar{t}} = \bar{\mu}\bar{v} \quad (24)$$

Using the velocity equation (17) with the conservation of angular momentum (12), the integrand of Eq. (23) can be written as a function of \bar{m} (or, equivalently, as a function of \bar{r}). The resulting integral does not admit a closed-form solution and an approximate solution can be obtained via numerical integration.

3. Case study

Relevant results in dimensional units related to the asteroid Bennu are here provided. Bennu has a mean radius $R = 262.5$ m, period 4.296 h and density $\rho = 1.26 \text{ g cm}^{-3}$ (i.e., $\bar{\omega} = 0.69$) Scheeres, Hesar, Tardivel, Hirabayashi, Farnocchia, McMahon, Chesley, Barnouin, Binzel, Bottke, Daly, Emery, Hergenrother, Lauretta, Marshall, Michel, Nolan and Walsh (2016). The radius of the spherical cavity that can be created inside Bennu extracting mass using a constant length siphon is $r_{f,max} = 66$ m (approximately one quarter of the outer radius), corresponding to a total extracted

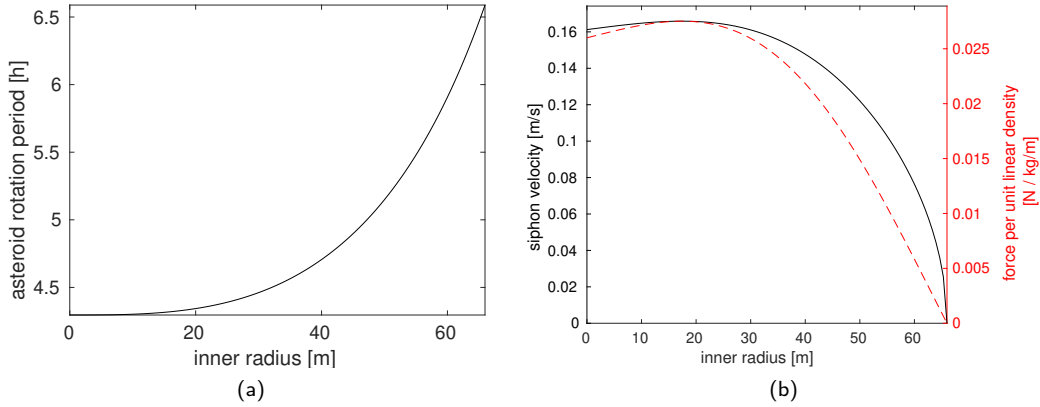


Figure 8: (a) Variation of Bennu rotation period as a function of the inner radius. (b) Siphon velocity (black) and force per unit linear density (red) as a function of the inner radius.

mass $m_f = 1.5 \times 10^9$ kg and requiring an optimal siphon length $L = 803$ m, approximately three times the radius of the asteroid. Figure 8a shows the variation of the asteroid period as a function of the inner radius using the conservation of angular momentum (Eq. (12)). The final asteroid period at the end of the manipulation process is approximately 1.5 larger than the initial period.

Figure 8b shows the radial velocity of the siphon (Eq. (17)) as a function of the radius of the inner cavity (black curve) as well as the siphon force per unit linear density f_{cont}/μ (red). The velocity is on the order of cm/s, comparable with previous results for a siphon anchored at the asteroid surface Viale et al. (2018a) and drops to zero towards the end of the manipulation process, when the radial force on the chain approaches zero and the siphon reaches its equilibrium state.

Figures 9a and 9b show the time required to generate a cavity with inner radius r and the average mass flow rate as a function of r , for a range of siphon linear densities μ . For example, a 27-meter radius cavity, corresponding to approximately 10^5 tonne of removed material, can be excavated in 6.2 years, for a siphon linear density $\mu = 1 \text{ kg m}^{-1}$, or 45 days, for $\mu = 50 \text{ kg m}^{-1}$. The required instantaneous mass rates are below 9 kg s^{-1} for $\mu \leq 50 \text{ kg s}^{-1}$ (Fig. 8b). Clearly, such mass rates depend upon the technology of mining units transferring material to the siphon and the physical properties of the asteroid. According to Sonter (1997), an equipment mass of 5 tonnes could process 1000 tonnes of asteroid regolith per day, or 11.5 kg s^{-1} which is larger than the maximum rate shown in Fig. 9b, suggesting that the siphon can be fed with the required mass rates for the test cases considered here. However, more detailed studies are required to calculate achievable mining throughput rates for the specific scenario discussed in this paper, by considering other key parameters neglected here, such as the number of mining rovers, rover locomotion speeds and the volume of material that each mining unit can transport.

As noted in Fig. 8a, the asteroid retains a residual angular velocity at the end of the manipulation process that cannot be further exploited if the siphon length is constant. However, by allowing the siphon length to increase, it is possible to leverage the residual rotational kinetic energy of the asteroid to further increase the volume of the internal cavity. For example, Fig. 10a shows the variation of the asteroid period as a function of the radius of the internal cavity when a siphon with variable length is used. The length L is chosen as a function of the equilibrium length, which increases during siphon operation (see Fig. 3). Figure 10b shows the length of the siphon as a function of the inner radius. The dotted vertical line represents the maximum radius of the inner cavity that can be excavated with a constant-length siphon. As expected, larger cavities can be created in this case. For example, taking $L = 1.2L_{\text{eq}}$, leads to a cavity with a radius of approximately 82 m. Clearly, when L is closer to the equilibrium length, larger cavities can be excavated. However, the case $L = L_{\text{eq}}$ represents an ideal limiting scenario, since the siphon would constantly experience zero net force by definition in

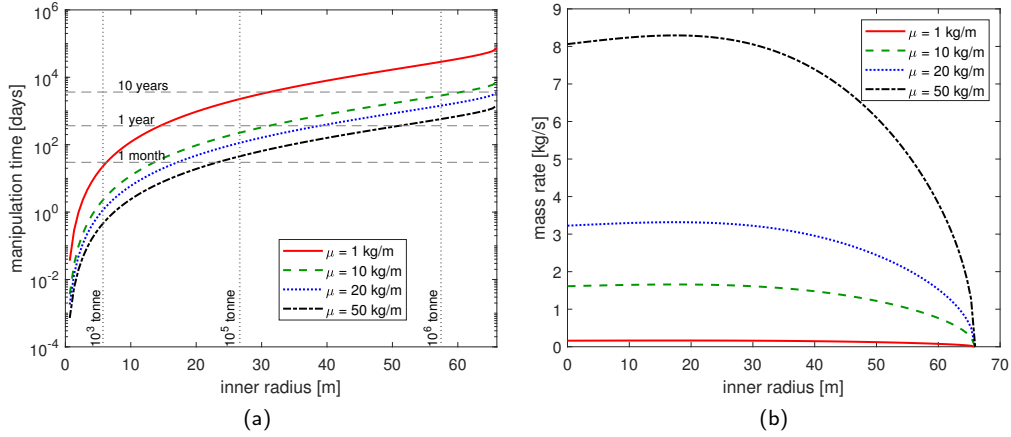


Figure 9: Manipulation time (a) (Eq. (23)) and instantaneous mass rate of lifted mass (b) (Eq. (24)) as a function of the inner radius r , for a range of siphon linear density μ .

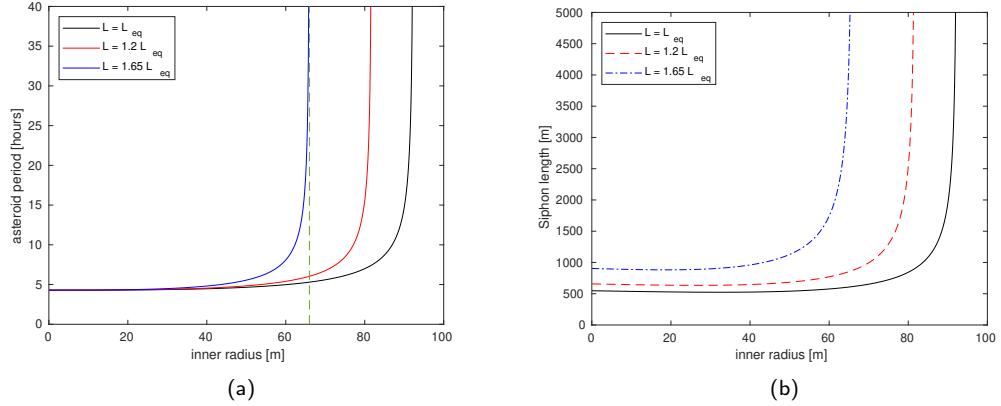


Figure 10: Variation of siphon period (a) and siphon length (b) for a variable-length siphon. The dotted vertical green line in Fig. 10a indicates the maximum radius of the internal cavity that can be excavated using a constant length siphon.

this case. The case $L = 1.65L_{eq}$ leads to an equivalent result as the constant length siphon case. Moreover, it should be noted that by changing the shape of the cavity, the angular velocity equation (21) would change accordingly, thus in principle changing the maximum extractable mass m_f and therefore the volume of the internal cavity. The key parameter here is the resulting inertia of the spherical asteroid with the internal cavity: if, for a given void volume, this parameter is maximised (or, in turn, the inertia of the cavity is minimised), then the angular velocity of the system comprising the asteroid and the siphon at the end of siphon operation is maximised, according to conservation of angular momentum and, therefore, a larger amount of mass can be extracted. For example, a cylinder with height h and cross section diameter d would have half the inertia of a sphere with diameter d if $h = 4/15d$. Although it is expected that the resulting cavity volumes will not change significantly from the values found in the present preliminary analysis for a spherical cavity, further studies are required to apply the present concept to different cavity shapes.

4. Analytical modelling of structural failure

As shown in the previous sections, the creation of a void in the interior of the asteroid alters the physical characteristics of the body: its rotation period increases due to conservation of angular momentum and its mass is reduced. Therefore, it is expected that the distribution of the internal stresses on the asteroid will change. In this section we use a simple analytical model developed using a continuum mechanics approach to explore the variation of the internal stresses due to the presence of an artificial cavity of variable size in the interior of the asteroid. Then, using the Drucker-Prager failure law [Chen and Han \(2007\)](#), the internal regions more sensitive to structural failure are identified.

A set of simplifying assumptions is made such that a closed form solution for the internal stresses can be found. Firstly, material behavior is assumed to be elastic-perfectly plastic, and therefore the effect of material hardening after yielding is not taken into account. The same spherical asteroid shape is assumed, as in the previous section. The only two body loads considered are those due to gravity and the asteroid rotation. The effects of the tunnel containing the siphon or that of any anchoring device are not considered in the derivation of the internal stresses. Also, it is assumed that the gradual increase of the inner cavity volume is quasi-static (so that any time-dependent change of the stress due to additional inertial forces is neglected) and any local variation of internal stress due to the interaction between mining units and the asteroid is not taken into account.

4.1. Elastic stress solution

A method described by Barber [Barber \(2002\)](#) is adapted to find a closed-form solution of the stress tensor on an axisymmetric body subjected to arbitrary axisymmetric tractions, in this case the self-gravity of the asteroid and centrifugal-induced force due to the asteroid rotation. Barber uses a method that involves harmonic functions to describe the displacement of the body. Eventually, through the stress-strain relationship, such displacements are then linked to the stresses.

Let $\mathcal{R}, \beta, \theta$ define a spherical coordinate system with origin at the asteroid center-of-mass, where \mathcal{R} is the radial distance from the centre, $\beta \in [0, \pi]$ is the co-latitude (with $\beta = 0, \beta = \pi$ being the latitude of the poles and $\beta = \pi/2$ being the latitude of the equator) and $\theta \in [0, 2\pi]$ is the longitude. Let σ_{ij} denote the stress tensor. A sufficiently general solution to σ_{ij} can be written in terms of the body force potential in the form ([Barber \(2002\)](#), p. 259 and 270):

$$\sigma_{\mathcal{R}\mathcal{R}} = \frac{\nu V}{1-\nu} + \frac{\partial^2 \phi}{\partial \mathcal{R}^2} + \mathcal{R} \cos \beta \frac{\partial^2 \psi}{\partial \mathcal{R}^2} - 2(1-\nu) \frac{\partial \psi}{\partial \mathcal{R}} \cos \beta + \frac{2\nu}{\mathcal{R}} \frac{\partial \psi}{\partial \beta} \sin \beta \quad (25a)$$

$$\sigma_{\theta\theta} = \frac{\nu V}{1-\nu} + \frac{1}{\mathcal{R}} \frac{\partial \phi}{\partial \mathcal{R}} + \frac{\cot \beta}{\mathcal{R}^2} \frac{\partial \phi}{\partial \beta} + \frac{\cos^2 \beta}{\mathcal{R} \sin \beta} \frac{\partial \psi}{\partial \beta} + (1-2\nu) \frac{\partial \psi}{\partial \mathcal{R}} \cos \beta + \frac{2\nu}{\mathcal{R}} \frac{\partial \psi}{\partial \beta} \sin \beta \quad (25b)$$

$$\sigma_{\beta\beta} = \frac{\nu V}{1-\nu} + \frac{1}{\mathcal{R}} \frac{\partial \phi}{\partial \mathcal{R}} + \frac{1}{\mathcal{R}^2} \frac{\partial^2 \phi}{\partial \beta^2} + \frac{\cos \beta}{\mathcal{R}} \frac{\partial^2 \psi}{\partial \beta^2} + (1-2\nu) \frac{\partial \psi}{\partial \mathcal{R}} \cos \beta + \frac{2(1-\nu)}{\mathcal{R}} \frac{\partial \psi}{\partial \beta} \sin \beta \quad (25c)$$

$$\sigma_{\beta\mathcal{R}} = \frac{1}{\mathcal{R}} \frac{\partial^2 \phi}{\partial \beta \partial \mathcal{R}} - \frac{1}{\mathcal{R}^2} \frac{\partial \phi}{\partial \beta} + \cos \beta \frac{\partial^2 \psi}{\partial \beta \partial \mathcal{R}} + (1-2\nu) \frac{\partial \psi}{\partial \mathcal{R}} \sin \beta - \frac{2(1-\nu)}{\mathcal{R}} \frac{\partial \psi}{\partial \beta} \cos \beta \quad (25d)$$

$$\sigma_{\theta\mathcal{R}} = \sigma_{\theta\beta} = 0 \quad (25e)$$

where ϕ and ψ are two potential functions satisfying

$$\nabla^2 \phi = \frac{(1-2\nu)V}{1-2\nu} \quad (26a)$$

$$\nabla^2 \psi = 0 \quad (26b)$$

and V is the body force potential. The conditions defined by Eqs. (26) ensure that the equilibrium equations are satisfied whereas Eqs. (25) represent the stress-strain relations, expressed as a function of the potentials ϕ and ψ (the interested reader is referred to [Barber \(2002\)](#) for additional details). The body potential V associated with the gravitational and rotational loads is, in spherical coordinates,

given by

$$V = \frac{4}{3}G\pi\rho^2 \left(\frac{1}{2}\mathcal{R}^2 + \frac{r^3}{\mathcal{R}} \right) - \frac{1}{2}\rho\mathcal{R}^2\omega^2 \sin^2 \beta \quad (27)$$

Traction-free boundary conditions are imposed at the outer and inner surface, i.e.

$$\sigma_{ij}(\mathcal{R} = r, \beta, \theta)\hat{n} = 0 \quad (28a)$$

$$\sigma_{ij}(\mathcal{R} = R, \beta, \theta)\hat{n} = 0 \quad (28b)$$

where \hat{n} is the normal to the surface. Therefore, the goal is to identify two harmonic functions ϕ and ψ that simultaneously satisfy: (i) the equilibrium equations given by Eqs. (26) and (ii) the boundary conditions (Eq. (28)) upon substitution on the stress-strain Eqs. (25). To this end, first note that the function ϕ can be decomposed in the sum $\phi_p + \phi_h$, representing the particular and homogenous solution to Eq. (26a) respectively. It can be easily verified that the particular solution

$$\phi_p = \frac{\mathcal{R}^4 \rho \omega^2 (1 - 2\nu)(5 \cos 2\beta - 3)}{280(1 - \nu)} + \frac{4}{3} \pi \rho G \rho^2 \frac{2\nu - 1}{\nu - 1} \left(\frac{\mathcal{R}^4}{40} + \frac{r^3 \mathcal{R}}{2} \right) \quad (29)$$

satisfies Eq. (26a). In order to find the homogeneous solutions ϕ_h and ψ , these are written in terms of spherical harmonics with coefficients to be found in order to satisfy the boundary conditions Eq. (28). In particular, the functions ϕ_h and ψ can be written as:

$$\phi_h = A_1 \mathcal{R}^{-1} + \frac{1 + 3 \cos \beta}{4} (A_2 \mathcal{R}^2 + A_3 \mathcal{R}^{-3}) + A_4 \mathcal{R}^4 \frac{9 + 20 \cos 2\beta + 35 \cos 4\beta}{64} \quad (30)$$

$$\psi = \cos \beta (B_1 \mathcal{R} + B_2 \mathcal{R}^{-2}) + B_3 \mathcal{R}^3 \frac{3 \cos \beta + 5 \cos 3\beta}{8} \quad (31)$$

where $A_1, A_2, A_3, A_4, B_1, B_2$ and B_3 are the coefficients to be determined. The specific spherical harmonics to be used are chosen to enable the boundary conditions to be satisfied. Substituting ψ and $\phi = \phi_p + \phi_h$ into Eqs. (25) and the imposing the boundary condition Eq. (28) forms a system of 7 linearly independent equations in the 7 unknowns $A_1, A_2, A_3, A_4, B_1, B_2$ and B_3 . Solving for the coefficients and then substituting the potentials ϕ, ψ back into Eqs. (25) permits the stress tensor σ_{ij} to be found. Scaling the stresses by the factor $4/3G\pi\rho^2\mathcal{R}^2$, the resulting stress tensor can be written as a function of $\bar{\omega}$, the Poisson ratio ν , the radial distance $\bar{\mathcal{R}}$ and the co-latitude β (due to the symmetry of the problem, the stress is independent of the longitude θ and it is symmetric with respect to the equatorial plane). The final solution is not explicitly reported here due to the length of the expressions. It is important to note that the particular case of $r = 0$ returns the classical solution for the stress field of an homogeneous elastic rotating sphere Kadish, Barber and Washabaugh (2005):

$$\sigma_{\mathcal{R}\mathcal{R}} = \frac{(\mathcal{R}^2 - 1) [5(2\nu^2 + \nu - 3)\omega^2 \cos 2\beta + 5\nu^2 + \nu(7\omega^2 - 8) + 9\omega^2 - 21]}{10(\nu - 1)(5\nu + 7)} \quad (32a)$$

$$\sigma_{\theta\theta} = \frac{-5(\nu^2 - 1)\mathcal{R}^2\omega^2 \cos 2\beta + \omega^2 [2\nu(5\nu - 1) + (\nu(5\nu + 14) + 13)\mathcal{R}^2 - 24]}{10(\nu - 1) - (5\nu + 7)} - \frac{\nu + (3\nu + 1)\mathcal{R}^2 - 3}{10(\nu - 1)} \quad (32b)$$

$$\sigma_{\beta\beta} = \frac{-5(2\nu^2 + \nu - 3)(\mathcal{R}^2 - 1)\omega^2 \cos 2\beta + \omega^2 [-7\nu + (\nu(10\nu + 19) + 3)\mathcal{R}^2 - 9]}{10(\nu - 1)(5\nu + 7)} - \frac{\nu + (3\nu + 1)\mathcal{R}^2 - 3}{10(\nu - 1)} \quad (32c)$$

$$\sigma_{\beta R} = -\frac{(2\nu + 3)(\mathcal{R}^2 - 1)\omega^2 \sin 2\beta}{2(5\nu + 7)} \quad (32d)$$

4.2. Failure law

Granular materials have zero or little tensile strength but can withstand considerable shear stress if under pressure. The pressure p is formally the average of the principal stresses $\sigma_1, \sigma_2, \sigma_3$, i.e., $p = (\sigma_1 + \sigma_2 + \sigma_3)/3$. Such pressure dependence is the consequence of the interlocking between the granular particles: in order to trigger failure, particles have to slide over one another and the confining pressure resist such motion Holsapple (2007). A common pressure-dependent criterion to assess failure of geological material is the Drucker-Prager criterion, which is formally an extension of the von-Mises criterion by introducing the influence of the pressure at failure. The Drucker-Prager model states that failure is achieved when Chen and Han (2007):

$$\alpha I_1 + \sqrt{J_2} - s \leq 0 \quad (33)$$

where I_1 and J_2 are the stress invariants

$$I_1 = \sigma_1 + \sigma_2 + \sigma_3 \quad (34)$$

$$J_2 = \frac{1}{6} [(\sigma_1 - \sigma_2)^2 + (\sigma_2 - \sigma_3)^2 + (\sigma_1 - \sigma_3)^2] \quad (35)$$

Note that I_1 is proportional to the pressure p ; the term $\sqrt{J_2}$ is related to the shear stresses Chen and Han (2007). The two coefficients α and s are macroscopic properties of the granular assembly. They can be related to the angle of friction ϕ and the cohesion c via Chen and Han (2007) :

$$\alpha = \frac{2 \sin \phi}{\sqrt{3}(3 - \sin \phi)} \quad (36)$$

$$s = \frac{6c \cos \phi}{\sqrt{3}(3 - \sin \phi)} \quad (37)$$

The cohesion is formally the shear strength at zero pressure. The angle of friction is associated with the interlocking between particles in the granular medium (see Ref. Chen and Han (2007)). Similar to Ref. Hirabayashi (2015) two types of cohesion are distinguished: the *actual* cohesion and the *critical cohesion* c^* . The former is a macroscopic property of the asteroid, the latter is defined as the value of the cohesion at which Eq. (33) is verified with the equality:

$$c^* = \frac{\sqrt{3}(3 - \sin \phi)}{6 \cos \phi} \sqrt{J_2} + \frac{1}{3} \tan \phi I_1 \quad (38)$$

The critical cohesion is an indicator of possible failure: if the actual cohesion c is smaller than c^* at any point on the asteroid interior, the asteroid may structurally fail.

4.3. Results

Following Ref. Hirabayashi (2015) the Poisson ratio is fixed at 0.25 and a range of angles of friction between 20 deg and 45 deg are considered. Figures 11 and 12 show the distribution of the non-dimensional critical cohesion \bar{c}^* in the xz plane at the beginning (left column) and at the end of siphon operation (right column), taking an angle of friction $\phi = 20$ deg and 45 deg respectively, for a range of initial angular velocity ($\bar{\omega}_0 = 0.6, \bar{\omega}_0 = 0.8, \bar{\omega}_0 = 1$). The final angular velocity and radius of the internal cavity are calculated with the method described in Sect 2.5 assuming constant and optimal siphon length, and their values are indicated in the title of each figure. The red dotted lines mark the contour lines characterized by $c^* = 0$ and a red dot indicates the location of $\max(\bar{c}^*)$ in the cases where $\max(\bar{c}^*) > 0$. Some relevant information can be inferred. When $r = 0$ the most sensible point is located on the outer surface of the asteroid for lower initial spin rates (at the poles for low angle of friction or at the equator for higher angles of friction) whereas it is at the center of

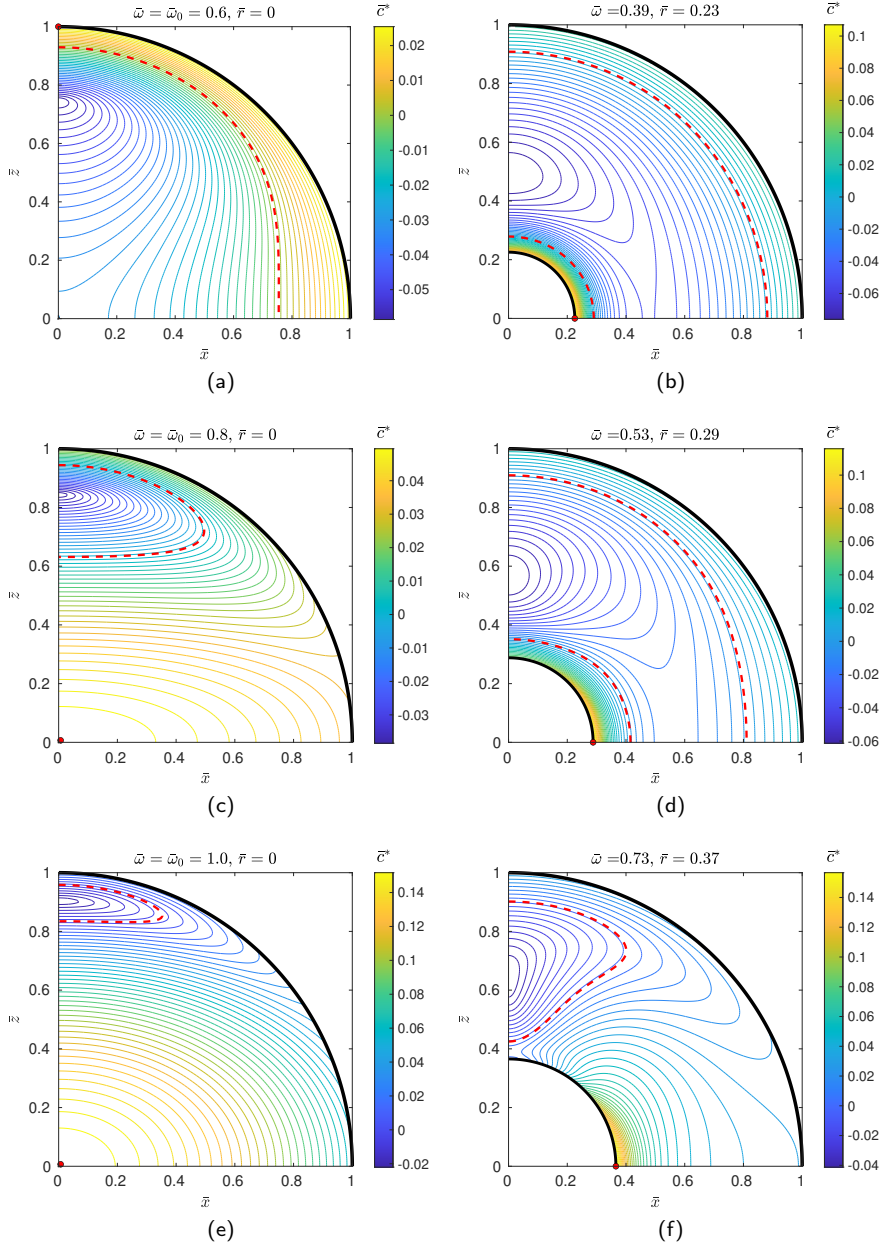


Figure 11: Non-dimensional critical cohesion \bar{c}^* at the beginning (left column) and the end (right column) of siphon operation, assuming a friction angle $\phi = 20$ deg.

the asteroid for higher spin rates. At low spin rates and large angles of friction the entire asteroid is characterized by negative stress (such as in the case $\omega_0 = 0.6$ and $\phi = 45$ deg), meaning that no cohesion is required for the asteroid to avoid structural failure. At the end of the manipulation process ($r > 0$), the location of the most sensible point is on the inner surface, in all the represented cases where $\max(\bar{c}^*) > 0$. At lower angular velocities, the distribution of the stresses does not strongly depend on the latitude. This result is expected since gravity is the predominant body force at slow spin rates. However, at larger angular velocities, the distribution of \bar{c}^* varies significantly with latitude and, for the cases represented here, the equator of the inner cavity is the point with highest sensitivity to failure.

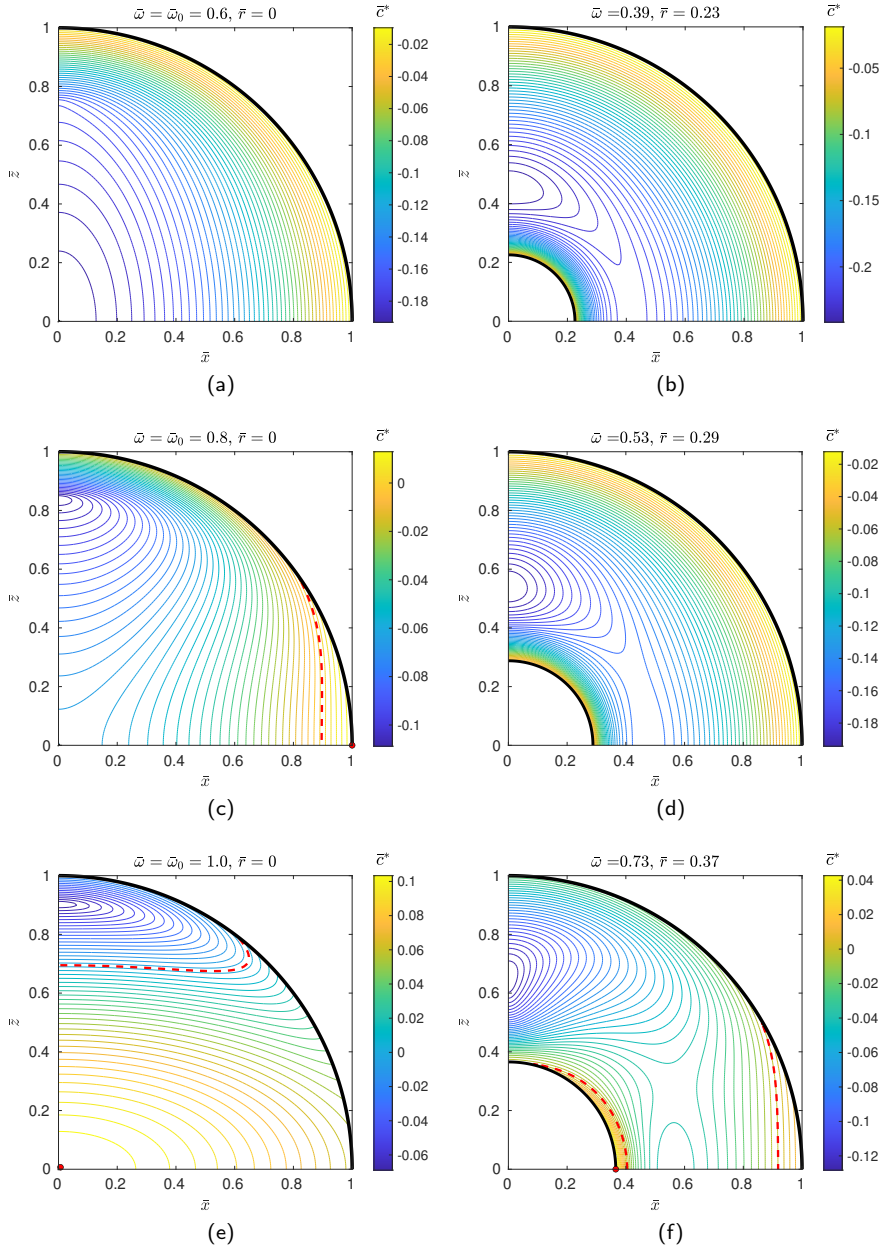


Figure 12: Non-dimensional critical cohesion \bar{c}^* at the beginning (left column) and the end (right column) of siphon operation, assuming a friction angle $\phi = 45$ deg.

Figure 13 shows the magnitude of the maximum critical cohesion (coloured contour curves) on the internal surface $\bar{R} = \bar{r}$ as function of the internal radius \bar{r} and the angular velocity, for $\phi = 25$ deg (a), $\phi = 35$ deg (b), $\phi = 40$ deg, $\phi = 45$ deg (d). Here, the critical cohesion is reported in dimensional units, assuming an asteroid with the same density and outer radius R as Bennu (details in Sect. 3). Also shown as dashed black curves is the variation of the angular velocity of the asteroid as a function of the inner radius considering the effect of the orbital siphon, for different initial angular velocities. Each dashed black curve is obtained via Eq. (21) taking a constant-length siphon, such that the final radius of the internal cavity is maximized. The right y-axis shows the period of the asteroid (the asteroid period $2\pi/\omega$ is completely defined from $\bar{\omega}$ if the asteroid density is fixed).

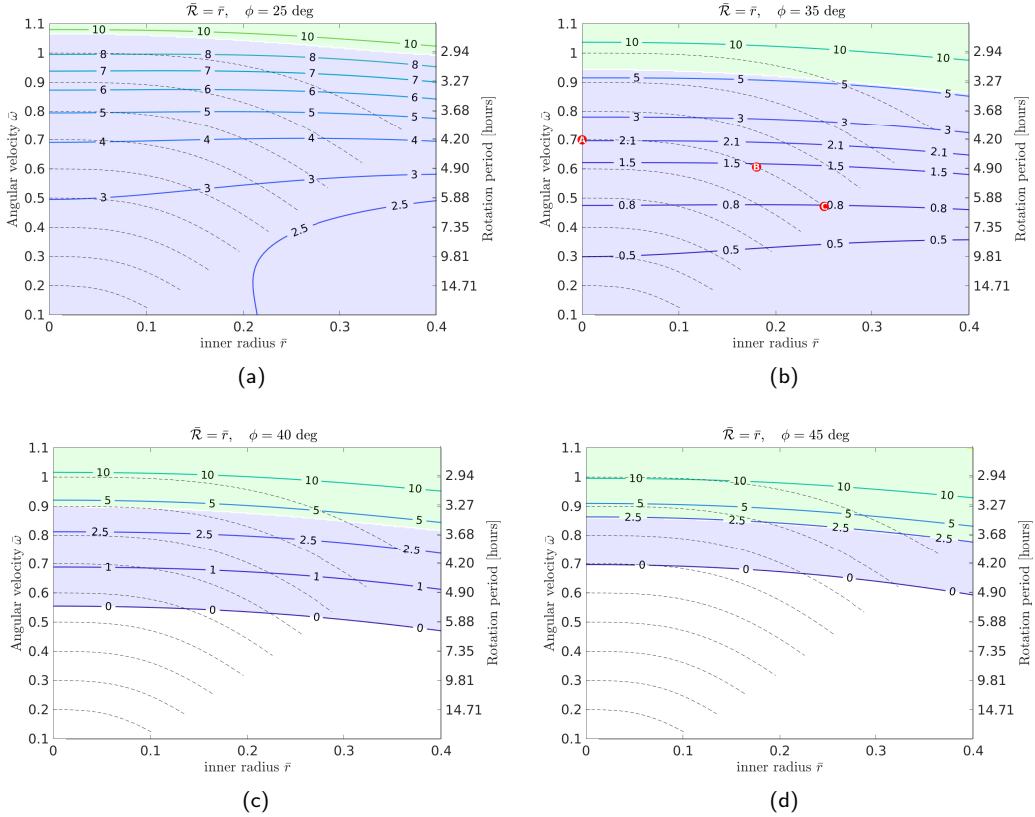


Figure 13: Contours of the maximum critical cohesion (in Pa) on the surface of the inner cavity $\mathcal{R} = r$ as a function of the inner radius and the asteroid angular velocity, for a range of angles of friction, as indicated in the title of each figure. The dashed black curve also show the variation of the asteroid angular velocity as a function of \bar{r} , for some values of $\bar{\omega}_0$. The shaded regions indicate the latitude of $\max(c^*)$ ($\max(c^*) > 0$): $\beta = 0$ (i.e., at the poles) for the green region and $\beta = \pi/2$ (i.e., at the equator) for the blue region. The right-hand y-axis shows the asteroid rotation period $2\pi/\omega$, taking an asteroid density $\rho = 1.26 \text{ g cm}^{-3}$. The three markers indicate the angular velocity for $\bar{r} = 0$ (A), beginning of siphon operation, $\bar{r} = 0.17$ (B) and $\bar{r} = 0.25$ (C), end of siphon operation.

Also, the shaded regions show the co-latitude at which the maximum critical cohesion is achieved (when $\max(c^*) > 0$): $\beta = 0$ (i.e., at the poles) for the green region and $\beta = \pi/2$ (i.e., at the equator) for the blue region. In general, the critical cohesion is not a strong function of the internal radius, since the contour lines are approximately horizontal (with some exceptions for low angular velocities and angle of friction, as in Fig. 13a). Therefore, since the angular velocity of the asteroid strictly decreases during siphon operation according to Eq. (21) (see the dashed black lines), it follows that the maximum critical cohesion c^* in the internal cavity decreases during the material removal process. For example, assuming an initial angular velocity $\omega_0 = 0.7$ and $\phi = 35$ deg (Fig. 13b) the critical cohesion at the beginning of siphon operation ($\bar{r} = 0$, marker A) is approximately 2.1 Pa, then it decreases to 1.5 Pa for $\bar{r} = 0.18$ (marker B) and eventually to 0.8 Pa at the end of siphon operation (marker C). This is consistent with the fact that both body loads (due to gravity and rotation) decrease during siphon operation and therefore the failure conditions are relaxed at larger r . If the initial asteroid angular velocity is close to the critical spin, the location of the most sensitive point changes from the poles to the equator of the internal cavity as r increases and this effect is most noticeable at larger angles of friction (see for example the black dashed line in Fig. 13c starting from $\bar{\omega} = 1$, intersecting both the green and the blue region). Figure 14 is equivalent to Fig. 13, however the

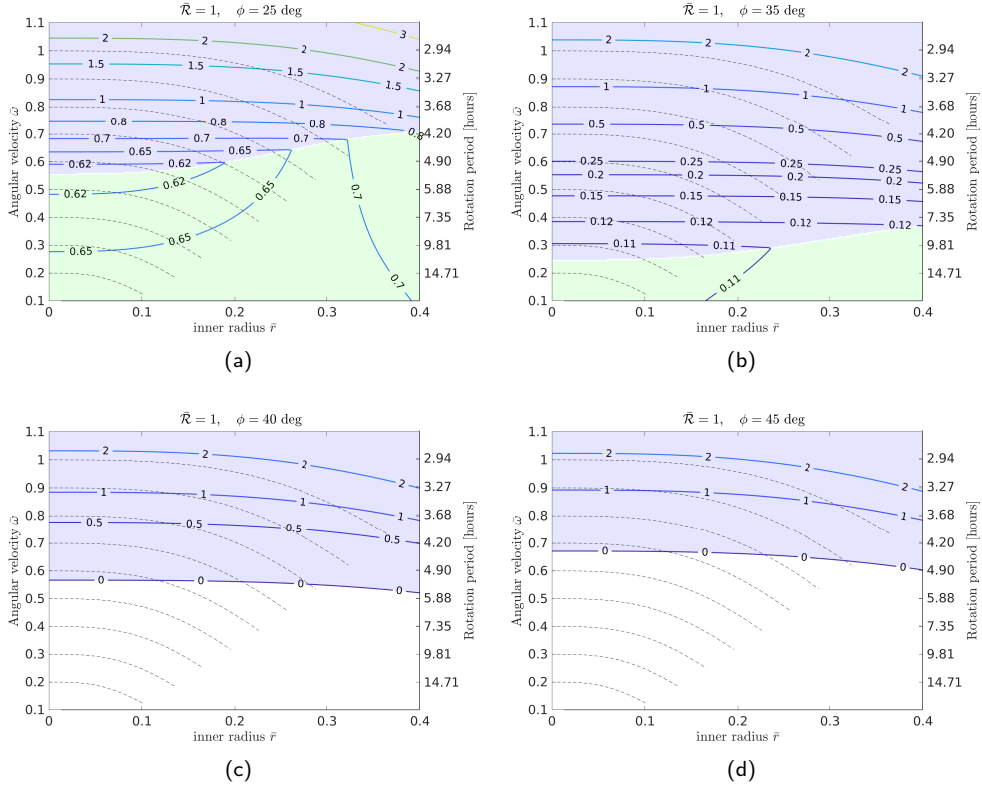


Figure 14: Contours of the maximum critical cohesion (in dimensional units, Pa) on asteroid surface $\bar{R} = R$ as a function of the inner radius and the asteroid angular velocity, for a range of angles of friction, as indicated in the title of each figure. The dashed black curve also show the variation of the asteroid angular velocity as a function of \bar{r} , for some values of $\bar{\omega}_0$. The shaded regions indicate the latitude of $\max(c^*)$ ($\max(c^*) > 0$): $\beta = 0$ (i.e., at the poles) for the green region and $\beta = \pi/2$ (i.e., at the equator) for the blue region. The right-hand y-axis shows the asteroid rotation period $2\pi/\omega$, taking an asteroid density $\rho = 1.26 \text{ g cm}^{-3}$.

contour of the maximum critical cohesion is calculated at the outer surface, $\bar{R} = 1$. As already suggested by Fig. 13 the maximum critical cohesion on the outer surface is always lower than the $\bar{R} = \bar{r}$ case. It can be verified this is true for any $\bar{r} < \bar{R} \leq 1$, thus confirming that the internal cavity is the most sensitive to failure. In general, at large angles of friction the asteroid equator is more sensitive to failure than the poles. Therefore, since the siphon operation does not increase the critical cohesive strength, the minimum level of cohesive strength the asteroid should have to avoid failure corresponds to the maximum critical cohesive strength for $r = 0$, at the beginning of siphon operation. For example, assuming an initial asteroid period equal to the nominal Bennu period (see Sect. 3), a minimum level of cohesion of approximately 4 Pa is required to avoid failure of the internal cavity. This is a conservative value calculated for $\phi = 25 \text{ deg}$ (Fig. 13a), however the requirement on the minimum cohesive strength is reduced for higher angles of friction.

Therefore, according to this preliminary model, the presence of the internal cavity does not challenge the structural stability of the asteroid as the cavity is generated. Further studies are then required to verify how external effects that were not taken into account in this model (e.g., siphon anchor forces, plastic behaviour of the asteroid material after yielding, stresses due to the mining rovers, non-spherical asteroid and cavity shape) may change the stress distribution.

5. Conclusion

In this paper it has been proposed to use the orbital siphon as a conveyor structure to create an artificial spherical cavity inside an asteroid. The siphon is a tethered mechanism which exploits the rotational self-energy of the asteroid to lift asteroid material to escape. It is shown that, for a Bennu-like asteroid, with a radius of 256 m and period 4.26 hour, a constant length siphon can be used to raise to escape 1.5×10^9 kg of asteroid material corresponding to an internal cavity with a diameter of 132 m, requiring a siphon with a length of 803 m. The time required to complete the manipulation process depends on the siphon linear density. For example, a siphon with a linear density of 20 kg s^{-1} can lift 10^6 tonnes of asteroid material to escape (corresponding to a 57-meter radius cavity) in approximately 10 years, with instantaneous mass rates smaller than 4 kg s^{-1} . Assuming elastic material behaviour, homogeneous internal structure and using a failure law for geological materials, it is shown the internal cavity is the region most sensitive to structural failure. However, as the internal cavity expands during siphon operation, the conditions for failure are relaxed. The required minimum cohesive strength to avoid failure is then evaluated at the beginning of siphon operation, and it is approximately 4 Pa for a Bennu-like asteroid.

Acknowledgements

CM is supported by a Royal Academy of Engineering Chair in Engineering Technologies and a Royal Society Wolfson Research Merit Award.

A. Conservation of angular momentum

- Step 1 \rightarrow 2 (Eq. (12a)). Substituting Eqs.(10) and (11) into Eq. (12a) and collecting MR^2 on both sides yields:

$$\frac{2}{5} \frac{1 - \bar{r}^5}{1 - \bar{r}^3} + \frac{\delta M}{M} \sum_{i=1}^n \bar{x}_i^2 = \left[\frac{2}{5} \frac{1 - \bar{r}^5}{1 - \bar{r}^3} + \frac{\delta M}{M} \sum_{i=1}^n (\bar{l} + \bar{x}_i)^2 \right] \left(1 - \frac{\delta \omega}{\omega} \right) \quad (39)$$

From $M = 4/3\rho\pi(R^3 - \bar{r}^3)$, it follows by differentiation:

$$\frac{\delta M}{M} = 3 \frac{\bar{r}^3}{1 - \bar{r}^3} \frac{\delta \bar{r}}{\bar{r}} \quad (40)$$

Substituting Eq. (40) into (39), neglecting higher order terms and further simplifying yields:

$$\frac{\delta \omega_{12}}{\omega_1} = 5 \frac{\bar{r}^5}{1 - \bar{r}^5} \left[\frac{3}{2} \left(1 + \frac{n\bar{l}}{\bar{r}} \right)^2 - \frac{1}{2} \right] \frac{\delta \bar{r}}{\bar{r}} \quad (41)$$

Assuming that the number of payloads is larger the term $n\bar{l}$ effectively represents the total length \bar{L} of the siphon:

$$\frac{\delta \omega_{12}}{\omega_1} = 5 \frac{\bar{r}^5}{1 - \bar{r}^5} \left[\frac{3}{2} \left(1 + \frac{\bar{L}}{\bar{r}} \right)^2 - \frac{1}{2} \right] \frac{\delta \bar{r}}{\bar{r}} \quad (42)$$

- Step 2 \rightarrow 3 (Eq. (12b)). Substituting Eqs. (10) and (11) into Eq. (12b) and collecting MR^2 on both sides yields:

$$\frac{2}{5} \frac{1 - \bar{r}^5}{1 - \bar{r}^3} + \frac{\delta M}{M} \sum_{i=1}^n \bar{x}_i^2 = \left[\frac{2}{5} \left(1 - \frac{\delta M}{M} \frac{1 - \bar{r}^5}{1 - \bar{r}^3} \left(1 + \frac{\delta \bar{r}}{\bar{r}} \right)^5 \right) + \frac{\delta M}{M} \sum_{i=1}^{n+1} (\delta \bar{r} + \bar{x}_i)^2 \right] \left(1 - \frac{\delta \omega}{\omega} \right)$$

Under the assumption $\delta\bar{r}/\bar{r} \ll 0$ it follows that

$$\frac{1 - \bar{r}^5 \left(1 + \frac{\delta\bar{r}}{\bar{r}}\right)^5}{1 - \bar{r}^3 \left(1 + \frac{\delta\bar{r}}{\bar{r}}\right)^3} = \frac{1 - \bar{r}^5}{1 - \bar{r}^3} \left[1 + \left(3 \frac{\bar{r}^3}{1 - \bar{r}^3} - 5 \frac{\bar{r}^5}{1 - \bar{r}^5} \right) \frac{\delta\bar{r}}{\bar{r}} \right] + o\left(\frac{\delta\bar{r}}{\bar{r}}\right) \quad (44)$$

Substituting Eqs.(40), (44) into Eq.(43), neglecting the higher order terms and further simplifying yields:

$$\frac{\delta\omega_{23}}{\omega_1} = -\frac{5}{2} \frac{\bar{r}^5}{1 - \bar{r}^5} \frac{\delta\bar{r}}{\bar{r}} \quad (45)$$

- Step 3 \rightarrow 4 (Eq. (12c)). The result follows immediately noting that $I_{A,3} = I_{A,4}$ and $I_{C,4} = I_{C,3} - \delta M(\bar{r} + (n-1)\bar{l})^2$:

$$\frac{\delta\omega_{34}}{\omega_1} = 0 \quad (46)$$

References

- Abramowitz, M., Stegun, I.A., 1964. Handbook of mathematical functions: with formulas, graphs, and mathematical tables. volume 55. Courier Corporation.
- Barber, J.R., 2002. Elasticity. Springer. doi:10.1007/0-306-48395-5.
- Chen, W.F., Han, D.J., 2007. Plasticity for structural engineers. J. Ross Publishing.
- Dunn, J., Fagin, M., Snyder, M., Joyce, E., 2017. Project rama: Reconstructing asteroids into mechanical automata .
- Gerlach, C.L., 2005. Profitably exploiting near-earth object resources. Proceedings of the 2005 International Space Development Conference, National Space Society, Washington DC. .
- Harris, L.R., Hersh, R., Hofhammer, T., Jenkin, M., 2014. How much gravity is needed to establish the perceptual upright? PLoS ONE 9, e106207. URL: <https://doi.org/10.1371/journal.pone.0106207>, doi:10.1371/journal.pone.0106207.
- Hennion, P., Mollard, R., 1993. An assessment of the deflecting effect on human movement due to the coriolis inertial forces in a space vehicle. Journal of Biomechanics 26, 85–90. URL: <https://doi.org/10.1016/j.jbiomech.1993.06.016>, doi:10.1016/0021-9290(93)90616-m.
- Hirabayashi, M., 2015. Failure modes and conditions of a cohesive, spherical body due to YORP spin-up. Monthly Notices of the Royal Astronomical Society 454, 2249–2257. URL: <https://doi.org/10.1093/mnras/stv2017>, doi:10.1093/mnras/stv2017.
- Holsapple, K.A., 2007. Spin limits of solar system bodies: From the small fast-rotators to 2003 EL61. Icarus 187, 500–509. URL: <https://doi.org/10.1016/j.icarus.2006.08.012>, doi:10.1016/j.icarus.2006.08.012.
- Kadish, J., Barber, J., Washabaugh, P., 2005. Stresses in rotating spheres grown by accretion. International Journal of Solids and Structures 42, 5322–5334. URL: <https://doi.org/10.1016/j.ijsolstr.2004.11.009>, doi:10.1016/j.ijsolstr.2004.11.009.
- Maindl, T.I., Miksch, R., Loibnegger, B., 2019. Stability of a rotating asteroid housing a space station. Frontiers in Astronomy and Space Sciences 6. URL: <https://doi.org/10.3389/fspas.2019.00037>, doi:10.3389/fspas.2019.00037.
- McInnes, C., 2017. Harvesting near Earth asteroid resources using solar sail technology. Fourth International Symposium on Solar Sailing (ISSS 2017), Kyoto, Japan, 17-20 Jan 2017 , 7.
- McInnes, C.R., Davis, C., 2005. Novel payload dynamics on space elevator systems. 56th International Astronautical Congress, IAC-05-D4.2-07 doi:10.2514/6.iac-05-d4.2.07.
- Newton, I., 1687. Philosophiae naturalis principia mathematica. volume 1. G. Brookman.
- O’Neill, G.K., O’Leary, B., 1977. Space-Based Manufacturing from Nonterrestrial Materials. American Institute of Aeronautics and Astronautics. doi:10.2514/4.865312.
- Pravec, P., Harris, A.W., 2000. Fast and slow rotation of asteroids. Icarus 148, 12–20. doi:10.1006/icar.2000.6482.
- Sanchez, J., McInnes, C., 2012. Assessment on the feasibility of future shepherding of asteroid resources. Acta Astronautica 73, 49–66. doi:10.1016/j.actaastro.2011.12.010.
- Saylor, J., Zolensky, M., Bodnar, R., Le, L., Schwandt, C., 2001. Fluid inclusions in carbonaceous chondrites. Lunar and Planetary Science XXXII 1.
- Scheeres, D., Hesar, S., Tardivel, S., Hirabayashi, M., Farnocchia, D., McMahon, J., Chesley, S., Barnouin, O., Binzel, R., Bottke, W., Daly, M., Emery, J., Hergenrother, C., Lauretta, D., Marshall, J., Michel, P., Nolan, M., Walsh, K., 2016. The

- geophysical environment of Bennu. *Icarus* 276, 116–140. URL: <https://doi.org/10.1016%2Fj.icarus.2016.04.013>, doi:10.1016/j.icarus.2016.04.013.
- Sonter, M., 1997. The technical and economic feasibility of mining the near-Earth asteroids. *Acta Astronautica* 41, 637–647. URL: <https://doi.org/10.1016%2Fs0094-5765%2898%2900087-3>, doi:10.1016/s0094-5765(98)00087-3.
- Viale, A., Ceriotti, M., McInnes, C., 2020a. Dynamics of an orbital siphon anchored to a rotating ellipsoidal asteroid for resource exploitation. *Acta Astronautica* URL: <https://doi.org/10.1016%2Fj.actaastro.2020.08.001>, doi:10.1016/j.actaastro.2020.08.001.
- Viale, A., McInnes, C., Bailet, G., Ceriotti, M., 2020b. Asteroid deflection by leveraging rotational self-energy. *Journal of Spacecraft and Rockets*.
- Viale, A., McInnes, C., Ceriotti, M., 2018a. Analytical mechanics of asteroid disassembly using the orbital siphon effect. *Proceedings of the Royal Society A: Mathematical, Physical and Engineering Sciences* 474, 20180594. doi:10.1098/rspa.2018.0594.
- Viale, A., McInnes, C., Ceriotti, M., 2020c. Dynamics of a nonrigid orbital siphon at a near-earth asteroid. *Journal of Guidance, Control, and Dynamics*, 1–15 URL: <https://doi.org/10.2514%2F1.g004894>, doi:10.2514/1.g004894.
- Viale, A., McInnes, C.R., Ceriotti, M., 2018b. Disassembly of near earth asteroids by leveraging rotational self energy. 69th International Astronautical Congress, IAC-18-D4.3-18, 13608–13617 URL: <http://eprints.gla.ac.uk/168724/>.